Low-energy electron elastic scattering and impact ionization with hydrogenlike helium in Debye plasmas

Jun Li,[1] Song Bin Zhang,[2,*] Bang Jiao Ye,[1,†] Jian Guo Wang,[3] and R. K. Janev[4]

[1]*State Key Laboratory of Particle Detection and Electronics, Department of Modern Physics, University of Science and Technology of China, 230026 Hefei, People's Republic of China*

[2]*School of Physics and Information Technology, Shaanxi Normal University, 710119 Xi'an, China*

[3]*Institute of Applied Physics and Computational Mathematics, P.O. Box 8009, Beijing 100088, China*

[4]*Macedonian Academy of Sciences and Arts, P.O. Box 428, 1000 Skopje, Macedonia*

(Received 17 April 2017; revised manuscript received 6 July 2017; published 11 September 2017)

Low-energy electron elastic scattering and impact ionization with hydrogenlike helium in Debye plasmas have been investigated by employing the exterior complex scaling method. The interactions between charged particles in the plasmas have been represented by Debye-Hückel potentials. The $1s$-$1s$ elastic collision strengths below the $n = 2$ excitation threshold of He^+ dominated by resonance structures are calculated for different screening lengths. As the screening strength increases, the resonance peaks studied [$_2(1,0)_2{}^+{}^1S^e$, $^3P^o$, $^1D^e$, and $_2(0,1)_2{}^+{}^1P^o$] exhibit blueshifts and then redshifts with a further increase of the screening strength, which results in dramatic changes of the collision strengths. It is found that these dynamic variation features of the resonances are related to the changes of energy levels of He^+ in the screened potential and geometric configurations of resonances. Triple-differential-ionization cross sections in coplanar geometries at 6-Ry incident electron energy are also reported, significant changes are observed with varying screening length.

DOI: 10.1103/PhysRevA.96.032707

I. INTRODUCTION

The electron-atom–ion collision processes in hot dense plasmas has attracted significant attention in recent decades in connection with the research in the fields of inertial confinement fusion, laser-produced plasmas, and astrophysics [1–3]. In hot dense plasmas the Coulomb interactions between charged particles are screened due to the collective effects of correlated many-particle interactions [1,2,4]. This results in changes of atomic electronic structures and collision dynamics of atomic processes in plasma environments [3,5,6]. The form of the screened interaction potential depends on the ratio of the average Coulomb interaction between plasma electrons and the average thermal plasma energy (coupling parameter) $\Gamma = \frac{e^2/\bar{a}}{k_B T_e}$, where e is the unit charge, $\bar{a} = (3/4\pi n_e)^{1/3}$ is the average distance between particles, k_B is the Boltzmann constant, n_e is the plasma electron density, and T_e is the temperature. In plasmas with $\Gamma \ll 1$ (weakly coupled classical or Debye plasmas) the screened interaction of an electron with a positive charge Ze is described by the Debye-Hückel potential [1,2,4]

$$V(r) = -\frac{Ze^2}{r}\exp(-r/D), \tag{1}$$

where $D = (k_B T_e/4\pi e^2 n_e)^{1/2}$ is the Debye screening length. The potential (1) describes the effects of many-particle interactions on the Coulomb interaction in the pairwise correlation approximation of the many-body correlation function.

When the coupling parameter is large ($\Gamma \geq 1$) the plasma-screened electron-ion interaction is often described by the ion sphere model potential (see, e.g., [2,7] and references therein). For cold and dense plasmas with $\Gamma \gg 1$, the plasma screening of Coulomb interactions is described with an exponential-cosine screened Coulomb potential (see [8,9] and references therein) that accounts for the electron degeneracy and correlation effects.

The most extensive theoretical studies of atomic structures and collision processes in weakly coupled, hot dense plasmas have so far been performed for one-electron systems by using the Debye-Hückel potential (1). These studies were recently reviewed in Ref. [10]. There have also been a significant number of studies devoted to the electronic structure of few-electron systems in the screened Coulomb potential (1). Hashino *et al.* have employed the variational method to study the bound states of heliumlike atoms in Debye plasmas in their early work [11]. Kar and Ho have investigated the effects of Debye plasmas on resonant states in electron–hydrogen-atom scattering (or hydrogen negative ion) and the doubly excited states of the helium atom and Ps^- ion by using the stabilization method [12–18]. They have also calculated the energies of bound states of helium atom in Debye plasmas by using the Rayleigh-Ritz variational method [19,20]. Doubly excited states of He in Debye plasmas have also been calculated by Chakraborty and Ho [21] employing the complex-coordinate rotation method, Lin *et al.* [22] using the configuration-interaction approach with B-spline basis functions, Ordóñez-Lasso *et al.* [23] using the Feshbach projection approach, and Jiao and Ho [24] employing the variational and complex-scaling methods. In contrast, Zhang *et al.* have studied the collision dynamics of low-energy electron–hydrogen-atom scattering in the screened Coulomb potential (1) by employing the R-matrix method with pseudostates (RMPS) [25–27]. Zammit *et al.* have calculated both the excitation and ionization processes in electron–hydrogen-atom collisions in Debye plasmas covering the energy range from threshold to high energies (250 eV) [28]. Whitten *et al.* have used the close-coupling and distorted-wave methods to study the plasma-screening effects on the electron-impact excitations of hydrogenlike ions with

*song-bin.zhang@snnu.edu.cn

†bjye@ustc.edu.cn

both the Debye-Hückel and ion sphere model potentials [6]. Note that the electronic structures of two-electron ions in dense quantum plasmas with exponential cosine screened potentials have also been studied [29–31].

While the collision dynamics of low-energy electron–hydrogen-atom scattering in Debye plasmas has been studied in detail by Zhang *et al.* [25–27], we are unaware of such a detailed study for an electron–hydrogenlike-ion collision system. The increased nuclear charge affects the change of the electron binding energy of the ion due to the plasma screening much more strongly than in the case of a hydrogen atom. This obviously affects the electron–hydrogenlike-ion collision dynamics. The aim of the present work is to study the modification in the elastic scattering and impact ionization processes in electron-He^+ collisions in Debye plasmas at low incident electron energies. The exterior complex scaling (ECS) method will be employed to investigate the effects of plasma screening on the resonances in the $1s$-$1s$ elastic collision strength below the $n = 2$ threshold of He^+ and on the triple-differential-ionization cross section in a number of coplanar geometries.

The organization of the article is as follows. In the next section we briefly describe the computational method. In Sec. III we present and discuss the results of our calculations. In Sec. IV our conclusions are summarized. Unless otherwise stated, atomic units (a.u.) are used throughout this work.

II. METHOD OF CALCULATION

The exterior complex scaling method has been described in detail elsewhere [32–34]. Its implementation to the electron–hydrogenlike-ion collisions (including He^+) has been illustrated in [34,35]. In this section we give only a brief outline of the ECS method for the electron–hydrogenlike-ion collision system. The total scattering wave functions $\psi^{LSM\Pi}_{l_1l_2}(r_1,r_2)$ are obtained by solving a set of biradial equations

$$(E-\hat{H}_1-\hat{H}_2)\psi^{LMS\Pi}_{l_1l_2}-\sum_{l'_1l'_2}\langle y^{LM}_{l_1l_2}|V_{12}|y^{LM}_{l'_1l'_2}\rangle\psi^{LMS\Pi}_{l'_1l'_2} = \chi^{LMS\Pi}_{l_1l_2}, \tag{2}$$

where E is the total energy of the three-body system. In addition, $\hat{H}_i$ is the single-electron Hamiltonian including the electron kinetic energy and electron-nucleus potential energy

$$\hat{H}_i = -\frac{1}{2}\nabla_i^2-\frac{Z}{r_i}, \tag{3}$$

where Z is the ion core charge ($Z = 2$ for He^+). In Eq. (2) V_{12} is the electron-electron interaction, $y^{LM}_{l_1l_2}$ are the coupled spherical harmonics [33,34,36], and $\chi^{LMS\Pi}_{l_1l_2}$ is the wave function of the initial state, which can be written as

$$\chi^{LMS\Pi}_{l_1l_2}(r_1,r_2) = \frac{1}{k_i}\sum_l\sqrt{2\pi(2l+1)}C^{LM}_{l_im_il0}i^l \times \exp[-i\sigma_l(Z-1,k_i)]\Bigg[\Bigg(\Bigg\langle l_1l_2\Bigg\|\frac{1}{r_{12}}\Bigg\|l_il\Bigg\rangle_L - \frac{1}{r_2}\delta^{l_i}_{l_1}\delta^{l}_{l_2}\Bigg)\phi_{n_il_i}(Z;r_1)\phi_l(Z-1;k_i,r_2) + (-1)^{S+\Pi}(1\leftrightarrow 2)\Bigg], \tag{4}$$

where k_i is the projectile electron momentum, $C^{LM}_{l_im_il0}$ is the Clebsch-Gordan coefficient, L and M are the total angular quantum number and its projection (both conserved in the collision process), respectively, l_i is the angular quantum number of the initial state of the bound electron in the hydrogenlike target, m_i is the pertinent magnetic quantum number, l is the partial wave of the projectile electron, and without loss of generality the incident electron is chosen along the z direction so that $m = 0$. In addition, $\phi_{n_il_i}(Z;r_1)$ is the initial-state wave function of the hydrogenlike target and $\phi_l(Z-1;k_i,r_2)$ and $\sigma_l(Z-1,k_i)$ are the Coulomb wave function and Coulomb phase shift, respectively. They describe the projectile electron in the Coulomb field of the hydrogenlike target. The last term in Eq. (4) represents the exchange between the projectile electron and the target electron, and S and Π are the total spin and parity of the system, respectively.

Generally, Eq. (2) can be completely solved by matching the wave functions of an inner radial region with the corresponding boundary conditions of an outer asymptotic region [33]. Many methods are based on this procedure, such as the R-matrix method [37], the convergent close-coupling method [38], and the time-dependent close-coupling method [39]. The ECS method avoids matching the solutions of the inner region to the sophisticated boundary conditions through a complex scaling of the real radial coordinates

$$R(r) = \begin{cases} r, & r < R_0 \\ R_0+(r-R_0)e^{i\theta_{\rm ECS}}, & r > R_0, \end{cases} \tag{5}$$

where R_0 is the turning point at which complex scaling begins and $\theta_{\rm ECS}$ is the rotation angle. In the complex scaling region $r > R_0$, the outward scattering wave function with complex scaling is exponentially damped. Thus the original sophisticated boundary conditions are replaced simply by zero in the ECS method. With the zero boundary conditions, the numerical scattering wave functions $\psi^{LMS\Pi}_{l_1l_2}$ in the $r < R_0$ region can be obtained and the scattering and ionization variables can be extracted by projecting them to the final states of the collision system. In the present calculations, the turning point R_0 was varied from 90 a.u. (for relatively high incident energies) to 200 a.u. (for relatively low incident energies) to ensure the convergence.

In the scattering excitation process, the scattering T matrix T^{LS}_l can be calculated by projecting $\psi^{LMS\Pi}_{l_1l_2}$ onto the final bound-continuum compound state

$$T^{LS}_l = \frac{1}{\sqrt{2}}\frac{4\pi}{k_f}i^{-l}\exp[i\sigma_l(Z-1,k_f)]C^{Lm_i}_{l_fm_flm_i-m_f} \times \lim_{R_0\to\infty}\int_0^{R_0}\phi_{n_fl_f}(Z;r_1) \times W\left[\psi^{LMS}_{l_fl}(r_1,r_2),\phi_l(Z-1;k_f,r_2)\right]_{R_0}dr_1, \tag{6}$$

where k_f is the momentum of the scattered electron in the final state, $\phi_{n_fl_f}(Z;r_1)$ is the wave function of the final bound state of the hydrogenlike target, $\phi_l(Z-1;k_f,r_2)$ and

$\sigma_l(Z-1,k_f)$ are the Coulomb wave function and Coulomb phase shift of the scattered electron, respectively, and $W[a,b]_{R_0} = a'(R_0)b(R_0) - a(R_0)b'(R_0)$ is the Wronskian. The integral cross section (ICS) can be obtained from the T matrix [40] and the complete cross section (CCS) is the sum of the ICS

$$\sigma_{fi} = \sum_{LS} \sigma_{fi}^{LS}, \quad \sigma_{fi}^{LS} = \frac{k_f}{k_i}\frac{2S+1}{4}\frac{1}{4\pi^2}\sum_{lL'} T_{fi,l}^{LS} T_{fi,l}^{L'S*}. \tag{7}$$

The relation between CCS and the collision strength Ω_{fi} is

$$\Omega_{fi} = \frac{k_i^2(2L_i+1)(2S_i+1)}{\pi a_0^2}\sigma_{fi}. \tag{8}$$

In the electron-impact ionization process, the entire ionization amplitudes can be calculated by projecting $\psi_{l_1l_2}^{LMS\Pi}$ to the continuum-continuum compound state

$$F^S(\mathbf{k}_1,\mathbf{k}_2) = \sum_{l_1l_2LM} i^{-l_1-l_2} e^{i(\sigma_{l_1}+\sigma_{l_2})} y_{l_1l_2}^{LM}(\hat{\mathbf{k}}_1,\hat{\mathbf{k}}_2) f_{l_1l_2}^{LMS}(k_1,k_2), \tag{9}$$

where

$$f_{l_1l_2}^{LMS}(k_1,k_2) = \frac{2}{\sqrt{\pi}}\frac{\rho}{k_1k_2}\int_0^{\pi/2}\left(\phi_{l_1}\phi_{l_2}\frac{\partial}{\partial\rho}\psi_{l_1l_2}^{LMS} - \psi_{l_1l_2}^{LMS}\frac{\partial}{\partial\rho}\phi_{l_1}\phi_{l_2}\right)d\alpha. \tag{10}$$

Here $\phi_{l_1}(Z;k_1,r_1)$ and $\phi_{l_2}(Z;k_2,r_2)$ are the Coulomb wave functions, σ_{l_1} and σ_{l_2} are the pertinent Coulomb phase shifts, $\rho = \sqrt{r_1^2+r_2^2}$, and $\alpha = \arctan(r_2/r_1)$ [33,34,36]. Finally, the ionization triple-differential-ionization cross section (TDCS), which contains the contributions of both the singlet and triplet two-electron states, can be deduced from the ionization amplitudes as

$$\frac{d\sigma}{d\hat{\mathbf{k}}_1 d\hat{\mathbf{k}}_2 dE_2} = \frac{d\sigma^{S=0}}{d\hat{\mathbf{k}}_1 d\hat{\mathbf{k}}_2 dE_2} + \frac{d\sigma^{S=1}}{d\hat{\mathbf{k}}_1 d\hat{\mathbf{k}}_2 dE_2} = \frac{1}{4}\frac{k_1k_2}{k_i}|F^{S=0}|^2 + \frac{3}{4}\frac{k_1k_2}{k_i}|F^{S=1}|^2. \tag{11}$$

Note that the ECS theory is independent of the interaction potentials; however, the initial and final states need to be exact for the given potentials. In the scattering of an electron with He^+ in Debye plasmas, both the electron-nucleus and electron-electron Coulomb interactions are screened. Explicitly, with the screened Coulomb potentials, the single-electron Hamiltonian is

$$H_i = -\frac{1}{2}\nabla_i^2 - \frac{Z}{r_i}\exp\left(-\frac{r_i}{D}\right) \tag{12}$$

and the electron-electron interaction is

$$V_{12} = \frac{1}{r_{12}}\exp\left(-\frac{r_{12}}{D}\right), \tag{13}$$

where $r_{12} = |\mathbf{r}_1 - \mathbf{r}_2|$ is the interelectron distance.

With the Hamiltonian (12), for the He^+ target in Debye plasmas the screened bound orbitals ϕ_{nl} are different from that in the pure Coulomb field. Similarly, the continuum states of the Hamiltonian (12) are not Coulomb wave functions anymore and ϕ_l and σ_l in Eqs. (4), (6), (9), and (10) need to be replaced by the continuum wave functions of the Debye-Hückel potential. In this work, the bound orbitals and continuum wave functions are numerically calculated by the RADIAL program [41]. The present ECS code is based on the modification of the packages hex-ecs [36] and hex-db [40].

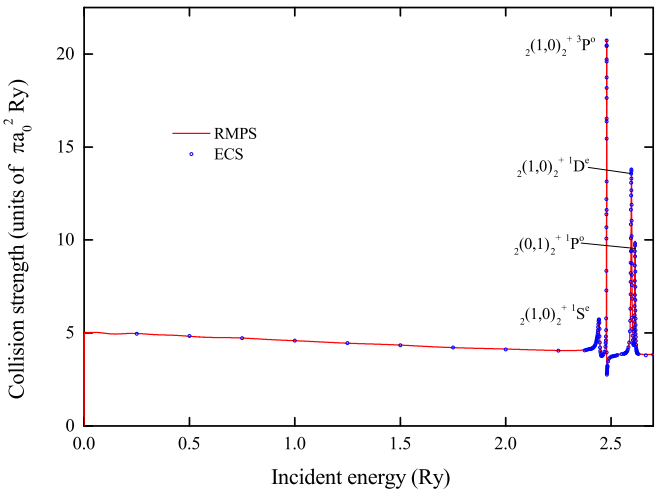

FIG. 1. The $1s$-$1s$ elastic collision strengths below the $n=2$ excitation threshold of He^+. The line shows the present RMPS results and the circles the present ECS results.

III. RESULTS AND DISCUSSION

A. The $1s$-$1s$ elastic collision strength

In order to verify the modification of the computer package, we have calculated the $1s$-$1s$ elastic collision strengths of e-He^+ scattering in the energy region below the $n=2$ threshold and compared with the RMPS result [42]. Good agreement is obtained as shown in Fig. 1. Four dominant resonant structures can be identified in the $1s$-$1s$ elastic collision strengths at the incident energies around 2.5 Ry. The resonance parameters (energy position and width) can be evaluated by fitting the eigenphase sum [26] from RMPS and are (in a.u.) $(-0.777\,810, 4.58\times10^{-3})$, $(-0.760\,461, 2.99\times10^{-4})$, $(-0.701\,610, 2.38\times10^{-3})$, and $(-0.692\,805, 1.37\times10^{-3})$) for the $2s^2\,{}^1S^e$, $2s2p\,{}^3P^o$, $2p^2\,{}^1D^e$, and $2s2p\,{}^1P^o$ resonances, respectively. The calculated resonance parameters agree very well with those published by other authors [23,43].

We note that the two-electron resonant states are more appropriately classified as ${}_n(K,T)_N{}^A$ and ${}^{2S+1}L^\pi$ in hyperspherical coordinates, as suggested by Lin [44–46]. Here L, S, and π are the usual quantum numbers of the whole system, n is the principal quantum number of the outer electron, and N is the principal number of the inner electron. In this notation A is the quantum number of radial correlations and indicates the distribution of the wave function in the hyperangle α; K and T are quantum numbers representing the angular correlations and contain the full information of the angular part $\Omega \equiv (\alpha,\hat{r}_1,\hat{r}_2)$. Within this classification, the four resonances observed in Fig. 1 have the notation

$_2(1,0)_2{}^+{}^1S^e$, $_2(1,0)_2{}^+{}^3P^o$, $_2(1,0)_2{}^+{}^1D^e$, and $_2(0,1)_2{}^+{}^1P^o$, respectively.

Before presenting e-He$^+$ elastic collision results in Debye plasmas by the present ECS method, we note that previously the authors have comprehensively studied the low-energy electron-hydrogen collision excitations in Debye plasmas by employing the modified RMPS method [25–27]. However, the RMPS cannot be successfully implemented in the present study due to the strong Coulomb field of the ion core. While the Debye-Hückel potential still decreases faster than the pure Coulomb potential of the nucleus at large distances, its short-range character is significantly weakened. The concept of a big radial box cannot be efficiently implemented in the R-matrix treatment [42], which presents difficulties in matching the correct wave functions in the outer radial region to the wave functions from the inner radial region. As mentioned in the preceding section, the ECS method avoids the difficult matching procedure by making a complex scaling and turns into an easy and appropriate method to be implemented.

The elastic collision strengths below the $n = 2$ excitation threshold of He$^+$ for a selected number of values of the screening length between $D = \infty$ and $D = 3$ a.u. are presented in Figs. 2 and 3. Note that the critical screening lengths, where the $2s$ and $2p$ states of He$^+$ merge into a continuum, are 1.61 and 2.27 a.u., respectively [47]. As the figures show, the values of the collision strengths are not very sensitive to the variation of the screening length, except in the energy regions of resonances for very small screening lengths. For example, the values of collision strengths around resonances $_2(1,0)_2{}^+{}^1S^e$ and $_2(1,0)_2{}^+{}^3P^o$ hardly change for all the selected screening lengths (3 a.u. $\leqslant D \leqslant \infty$) (cf. Fig. 2). However, the peak of the $_2(1,0)_2{}^+{}^1D^e$ resonance decreases significantly when $D = 3.5$ a.u., where this resonance crosses over the He$^+(2s)$ threshold (cf. Fig. 3).

The most prominent features revealed in the figures are the variations of the resonant positions with decreasing the screening length. As shown in Fig. 2, the relative energy difference for resonances $_2(1,0)_2{}^+{}^1S^e$ and $_2(1,0)_2{}^+{}^3P^o$ is not sensitive to the variations of the screening length. Similarly, the relative energy differences for resonances $_2(1,0)_2{}^+{}^1S^e$, $_2(1,0)_2{}^+{}^3P^o$, and $_2(1,0)_2{}^+{}^1D^e$ hardly change for all the selected screening lengths, which agrees very well with the structure calculations for those resonances in Refs. [15,23] (see Fig. 4 for the variation of resonant positions with the screening length). With the decrease of screening length, resonances $_2(1,0)_2{}^+{}^1S^e$, $_2(1,0)_2{}^+{}^3P^o$, and $_2(1,0)_2{}^+{}^1D^e$ keep shifting towards the higher-energy region (blueshift) up to $D \approx 5$ a.u. However, with the further decrease of D, the resonance positions start to shift towards the lower energies (redshift). While the resonance $_2(0,1)_2{}^+{}^1P^o$ shows the same dynamic feature (blueshift to redshift reversal) when D varies, its critical screening length for this reversal is about $D \approx 6$ a.u. It is observed in Fig. 3 that for $D = 6$ a.u. the positions of resonances $_2(1,0)_2{}^+{}^1D^e$ and $_2(0,1)_2{}^+{}^1P^o$ almost coincide and their contributed (two) peak structures merge into one peak structure in the collision strength.

The dynamic variation features of the resonant positions [relative to the level He$^+(1s)$] in screened potentials can be understood from the changes of energy levels of He$^+$ in the screened potential and the geometric configurations

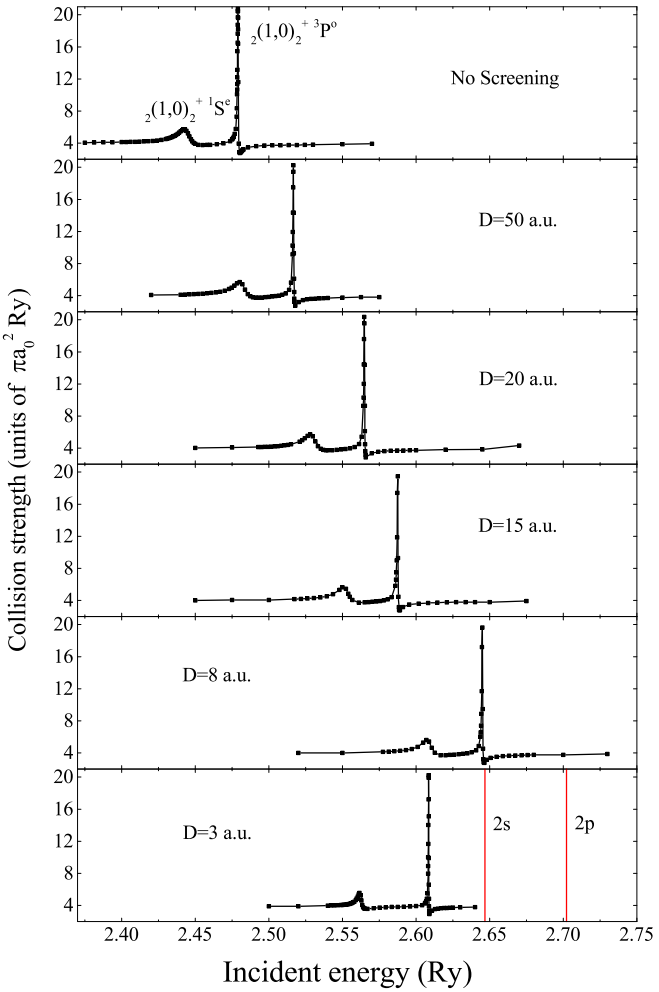

FIG. 2. Variations of resonances $^1S^e$ and $^3P^o$ manifested in the $1s$-$1s$ elastic collision strengths in Debye plasmas for different screening lengths. The vertical lines indicate the excitation energies for states $2s$ and $2p$ for the specific screening length D.

of the resonances in the hyperspherical coordinate representation. Figure 4 shows the dynamic variation of resonant positions (data from Refs. [15,23]), together with the energy differences between the energy levels of He$^+(n = 2)$ and He$^+(n = 1)$ for different screening lengths. Since the lower orbitals $2l(l = s, p)$ of He$^+$ (and other hydrogenlike ions) are tightly bound, from a very naive picture, the orbitals of the two electrons in the present studied resonances (doubly excited states $2l'2l''$ of He) should be close to orbitals $2l$ of He$^+$ with orbital energy $E_{\mathrm{He}^+(2l)}$, i.e., the energy of the resonance equals approximately to the orbital energies of the two electrons $(E_{\mathrm{He}^+(2l')} + E_{\mathrm{He}^+(2l'')})$ corrected with the electron-electron interaction (V_{ee}). It is apparent that this simple picture can break down quickly for higher orbitals of hydrogenlike ions and for any orbital of the hydrogen negative ion. As shown in Fig. 4, the relative energy differences $\Delta E = E_{\mathrm{He}^+(2l')} + E_{\mathrm{He}^+(2l'')} - E_{\mathrm{He}^+(1s)}$ increase with decreasing D down to $D \approx 3.5$ a.u. and then decrease with a further decrease of D, due to the rapid decrease of the electron-electron interaction V_{ee} with an increase of the screening strength. These changes result in the phenomenon of a blueshift to

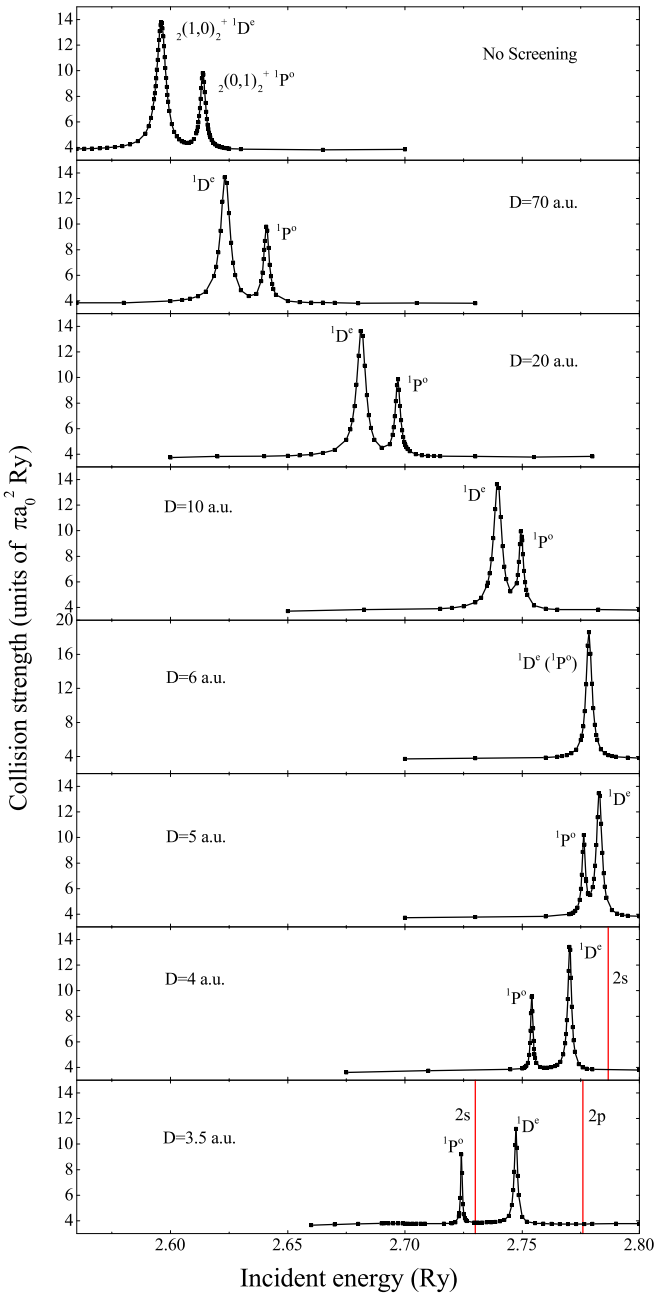

FIG. 3. Same as in Fig. 2 but for resonances $^1D^e$ and $^1P^o$.

redshift reversal of the resonant positions when D varies, observed in Figs. 2 and 3.

It is known that in the hyperspherical coordinate representation, the resonances $_2(1,0)_2{}^+\,{}^1S^e$, $_2(1,0)_2{}^+\,{}^3P^o$, and $_2(1,0)_2{}^+\,{}^1D^e$ possess the same geometric configurations and their positions show the same dynamic variation when D varies. For different geometric configurations, $K = 0$ [for resonances $_2(0,1)_2{}^+\,{}^1P^o$] signifies that the two electrons are in perpendicular orbitals, while $K = 1$ [for resonances $_2(1,0)_2{}^+\,{}^1S^e$, $_2(1,0)_2{}^+\,{}^3P^o$, and $_2(1,0)_2{}^+\,{}^1D^e$] signifies that the two electrons are separately localized on each side of the nucleus [45]. For the states with the same orbitals ($n = N = 2$) and different K, the electron-electron distance of the states with $K = 1$ is larger than that with $K = 0$; hence,

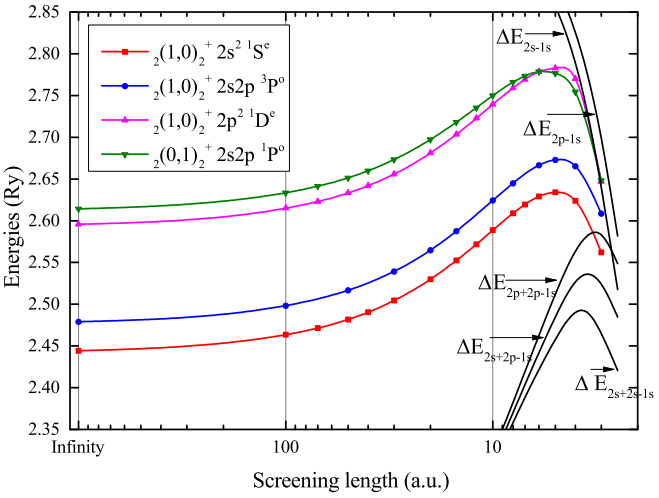

FIG. 4. Variations of the resonant positions ($^1S^e$, $^3P^o$, $^1D^e$, and $^1P^o$) and the energy differences ($\Delta E_{nl-n'l'} = E_{nl} - E_{n'l'}$ and $\Delta E_{nl+n'l'-n''l''} = E_{nl} + E_{n'l'} - E_{n''l''}$) between levels He^+ ($2s/2p$) and He^+ ($1s$) in Debye plasmas for different screening lengths. The resonant positions are cited from Ref. [23] for $^1S^e$, $^1D^e$, and $^1P^o$ and from Ref. [15] for $^3P^o$.

the electron-electron interaction in the states with $K = 1$ is smaller than that with $K = 0$. This results in the fact that the critical screening length for the blueshift to redshift reversal of the resonance $_2(0,1)_2{}^+\,{}^1P^o$ is larger than that of resonances $_2(1,0)_2{}^+\,{}^1S^e$, $_2(1,0)_2{}^+\,{}^3P^o$, and $_2(1,0)_2{}^+\,{}^1D^e$. We also note that in the previous studies of resonances in He and He-like positive ions [48–52] similar blueshift to redshift reversal phenomena were identified with the decrease of screening length and can be understood within the present qualitative model.

B. Triple-differential-ionization cross section

The present TDCSs for e-He^+ and e-H ionization with respective incident electron energies E_{inc} of 6 and 1.5 Ry in pure Coulomb interactions have been calculated in four different coplanar geometries [32,35]. The good agreement (not shown) observed with previous ECS calculations [35] validates our implementation. This work studies e-He^+ impact ionizations in the same geometries implemented in Ref. [35]. The present TDCS results for e-He^+ impact ionizations with fixed $E_{inc} = 6$ Ry in the selected coplanar geometries with screening lengths $D = \infty$, 100, 50, 20, 12, 8, and 5 a.u. are shown in Fig. 5. The energies of the outgoing electrons are E_1 and E_2 and their total energy is $E = E_{inc} + E_{n=1}(He^+) = E_1 + E_2$. Further, θ_1(or θ_2) is the relative outgoing angle to the direction of incident electron [35].

The TDCS features observed in the present unscreened case can be partly interpreted on the basis of the binary $(e, 2e)$ spectroscopy [53,54]. Thus, for $E_1 = 0.05E$ and $\theta_2 = 15^\circ$ [Fig. 5(a)], the forward peak around $\theta_1 \sim -90^\circ$ is mainly due to the single-binary (incident-target electron) collision, while the backward peak around $\theta_1 \sim 160^\circ$ is mainly due to the double-binary (incident electron–bound electron–nucleus) collision. The dip around $\theta_1 \sim 0^\circ$ is due to the interference of the single- and double-binary-collision scattering amplitudes. For the case of $E_1 = 0.95E$ and $\theta_2 = 15^\circ$ [Fig. 5(b)], the

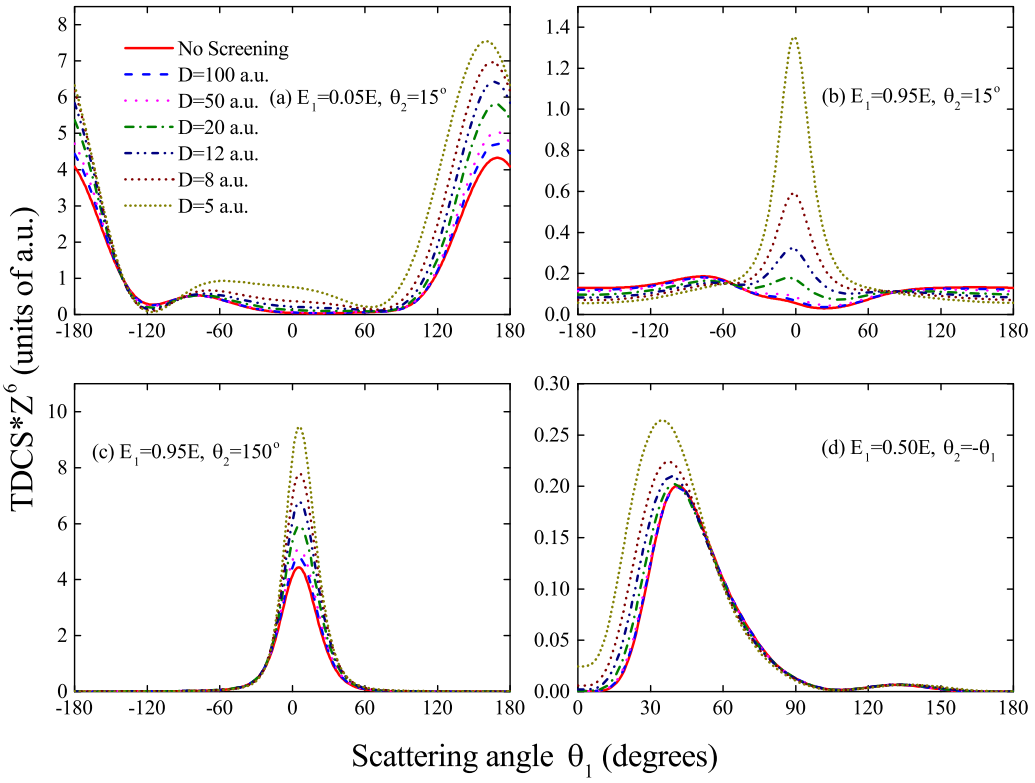

FIG. 5. Triple-differential cross sections of He^+ for the incident electron energy of 6 Ry in Debye plasmas in the selected coplanar geometries. The kinetic energy of the outgoing electron and the direction of the ejected electron are (a) $E_1 = 0.05E$ and $\theta_2 = 15^\circ$, (b) $E_1 = 0.95E$ and $\theta_2 = 15^\circ$, (c) $E_1 = 0.95E$ and $\theta_2 = 150^\circ$, and (d) $E_1 = 0.50E$ and $\theta_2 = -\theta_1$, respectively; E is the total energy of the whole collision system; and the ratio between E_1/E_2 in each panel for different screening lengths is fixed.

forward and backward peaks are greatly reduced, but the interference of the single- and double-binary-collision scattering amplitudes still produces a remarkable dip in the TDCS at $\theta_1 \sim 0^\circ$. For $E_1 = 0.95E$ and $\theta_2 = 150^\circ$ [Fig. 5(c)], the single-binary-collision mechanism completely dominates the process and the forward peak appears at $\theta_1 \approx 0^\circ$. In the symmetric equal energy sharing geometry [Fig. 5(d)], the forward peak at $\theta_1 \sim 45^\circ$ is again dominated by the single-binary-collision mechanism, whereas the double-binary-collision mechanism is responsible for the weak peak at $\theta_1 \sim 135^\circ$. We note that the process of single-binary collisions is almost independent of the nucleus, which is an important participant in the double-binary-collision process, and the momentum transferred in the single-binary collision is less than that in the double-binary collision.

As the figure shows, the TDCSs change significantly due to the screening effects. In the case with $E_1 = 0.05E$ and $\theta_2 = 15^\circ$, as shown in Fig. 5(a), with decreasing screening length, the amplitude of the backward peak increases and its position shifts towards smaller scattering angles; the position of the forward peak, on the other hand, is practically unaffected. In the case of Fig. 5(b) with $E_1 = 0.95E$ and $\theta_2 = 15^\circ$, the potential screening results in the emergence of a prominent forward peak around $\theta_1 = 0^\circ$ whose amplitude increases dramatically as the screening strength increases. In the case of Fig. 5(c) with $E_1 = 0.95E$ and $\theta_2 = 150^\circ$, the screened potential does not affect the peak structure considerably, but the peak amplitude increases dramatically with the decrease of the screening length. In the case of Fig. 5(d) with $E_1 = 0.50E$ and $\theta_2 = -\theta_1$, when the screening length decreases, the forward peak shifts towards smaller scattering angles and its amplitude increases significantly, while the screening effects hardly affect the backward peak.

In the environment of plasmas, the short-range character of the Debye-Hückel potential decreases the strong and complex interactions between the electrons and target and can provide a simpler picture to qualitatively understand the dynamic variations of the TDCS with the decrease of the screening length. The screened Coulomb potential decreases the electron-electron repulsive interactions and the ionization process can be treated as the classical two-ball collisions in the limit of very strong screening in which the electron-electron interactions can be neglected. In the classical two-ball collisions, both balls tend to move along the direction of the incident ball after collisions and both ionized and scattered electrons tend to escape along the direction of the incident electron ($\theta_{1,2} \to 0^\circ$). As revealed in Fig. 5 and described in the preceding paragraph, the shifting of the peak structures of TDCSs towards smaller scattering angles with the decrease of the screening length is consistent with the classical two-ball collisions. Note that in Fig. 5(b), $\theta_2 = 15^\circ$ is fixed and the newly appearing peaks for the screened case are around $\theta_1 \approx 0^\circ$ and along the direction of the incident electron; less electron-electron repulsion can weakly change the movement of the ionized (scattered) electron and increase the probability of the ionized (scattered) electron in a specific

direction. Furthermore, the TDCSs wholly increase, which is also consistent with the general increase of the TDCSs with the increase of the screening effects.

IV. CONCLUSION

In the present work we have studied the elastic scattering and impact ionization processes for e-He^+ collisions in Debye plasmas by the ECS method. In the low-energy elastic scattering process, the collision strengths are dominated by resonance structures. While the magnitudes of collision strengths are little affected by the screening effects of the plasma on the strength of the potential, these effects are dramatic in the energy positions of the resonances. With a decrease in screening length from $D = \infty$ to about 5 and 6 a.u. [for the resonances $_2(1,0)_2{}^+$ and $_2(0,1)_2{}^+$, respectively], the resonance positions shift towards the higher energies (blue shift), whereas with a further decrease of the screening length they shift towards the lower energies (redshift). An explanation for this blueshift to redshift reversal phenomenon is provided, based on a simple picture of the change of He^+ energy levels in Debye plasmas. It is argued that the difference in the critical screening lengths for the resonances $_2(1,0)_2{}^+$ and $_2(0,1)_2{}^+$, where this shift reversal occurs, originates from the different geometric configurations of the resonances.

The calculated TDCSs for the e-He^+ ionization process in Debye plasmas at an incident energy of 6 Ry and for four selected typical coplanar geometries also show significant differences with respect to the pure Coulomb results. The differences are particularly pronounced in the amplitudes and positions of forward and backward peaks of the cross sections, which are sensitive to the value of the screening length of Debye-Hückel potentials. Explanations for these differences were briefly discussed.

ACKNOWLEDGMENTS

J.L. thanks Jakub Benda for his detailed instructions of the packages hex-ecs and hex-db. B.J.Y. was partly supported by NSFC (Grants No. 11475165 and No. 11527811). S.B.Z. was partly supported by Shaanxi Normal University, the Organization Department of CCCPC, NSFC (Grant No. 11604197) and the Science Challenge Program of China (Grant No. TZ2016005).

[1] M. S. Murillo and J. C. Weisheit, Phys. Rep. **302**, 1 (1998).
[2] D. Salzmann, *Atomic Physics in Hot Plasmas* (Oxford University Press, Oxford, 1998).
[3] J. C. Weisheit, Adv. At. Mol. Phys. **25**, 101 (1989).
[4] J. P. Hansen and I. R. McDonald, *Theory of Simple Liquids* (Academic, London, 1986).
[5] H. Margenau and M. Lewis, Rev. Mod. Phys. **31**, 569 (1959).
[6] B. L. Whitten, N. F. Lane, and J. C. Weisheit, Phys. Rev. A **29**, 945 (1984).
[7] F. Rosmej, K. Bennadji, and V. S. Lisitsa, Phys. Rev. A **84**, 032512 (2011).
[8] P. K. Shukla and B. Eliasson, Phys. Lett. A **372**, 2897 (2008).
[9] L. G. Stanton and M. S. Murillo, Phys. Rev. E **91**, 033104 (2015).
[10] R. K. Janev, S. B. Zhang, and J. G. Wang, Matter Radiat. Extremes **1**, 237 (2016).
[11] T. Hashino, S. Nakazaki, T. Kato, and H. Kashiwabara, Phys. Lett. A **123**, 236 (1987).
[12] S. Kar and Y. K. Ho, New J. Phys. **7**, 141 (2005).
[13] S. Kar and Y. K. Ho, Chem. Phys. Lett. **402**, 544 (2005).
[14] S. Kar and Y. K. Ho, Phys. Rev. A **72**, 010703 (2005).
[15] S. Kar and Y. K. Ho, J. Phys. B **39**, 2445 (2006).
[16] S. Kar and Y. K. Ho, Int. J. Quantum Chem. **110**, 993 (2010).
[17] S. Kar and Y. K. Ho, Phys. Rev. A **71**, 052503 (2005).
[18] S. Kar and Y. K. Ho, Phys. Rev. A **73**, 032502 (2006).
[19] S. Kar and Y. K. Ho, Int. J. Quantum Chem. **106**, 814 (2006).
[20] S. Kar and Y. K. Ho, Int. J. Quantum Chem. **107**, 353 (2007).
[21] S. Chakraborty and Y. K. Ho, Eur. Phys. J. D **49**, 59 (2008).
[22] Y. C. Lin, C. Y. Lin, and Y. K. Ho, Phys. Rev. A **85**, 042516 (2012).
[23] A. F. Ordóñez-Lasso, J. C. Cardona, and J. L. Sanz-Vicario, Phys. Rev. A **88**, 012702 (2013).
[24] L. G. Jiao and Y. K. Ho, Phys. Rev. A **90**, 012521 (2014).
[25] S. B. Zhang, J. G. Wang, and R. K. Janev, Phys. Rev. Lett. **104**, 023203 (2010).
[26] S. B. Zhang, J. G. Wang, and R. K. Janev, Phys. Rev. A **81**, 032707 (2010).
[27] S. B. Zhang, J. G. Wang, R. K. Janev, and X. J. Chen, Phys. Rev. A **83**, 032724 (2011).
[28] M. C. Zammit, D. V. Fursa, and I. Bray, Phys. Rev. A **82**, 052705 (2010).
[29] L. U. Ancarani and K. V. Rodriguez, Phys. Rev. A **89**, 012507 (2014).
[30] A. Ghoshal and Y. K. Ho, J. Phys. B **42**, 175006 (2009).
[31] A. Ghoshal and Y. K. Ho, J. Phys. B **42**, 075002 (2009).
[32] T. N. Rescigno, M. Baertschy, W. A. Isaacs, and C. W. McCurdy, Science **286**, 2474 (1999).
[33] C. W. McCurdy, M. Baertschy, and T. N. Rescigno, J. Phys. B **37**, R137 (2004).
[34] P. L. Bartlett, J. Phys. B **39**, R379 (2006).
[35] P. L. Bartlett and A. T. Stelbovics, Phys. Rev. A **69**, 040701 (2004).
[36] J. Benda and K. Houfek, Comput. Phys. Commun. **185**, 2903 (2014).
[37] P. G. Burke, *R-Matrix Theory of Atomic Collisions: Application to Atomic, Molecular and Optical Processes* (Springer, Heidelberg, 2011).
[38] I. Bray and A. T. Stelbovics, Phys. Rev. A **46**, 6995 (1992).
[39] M. S. Pindzola, F. Robicheaux, S. D. Loch, J. C. Berengut, T. Topcu, J. Colgan, M. Foster, D. C. Griffin, C. P. Ballance, D. R. Schultz, T. Minami, N. R. Badnell, M. C. Witthoeft, D. R. Plante, D. M. Mitnik, J. A. Ludlow, and U. Kleiman, J. Phys. B **40**, R39 (2007).
[40] J. Benda and K. Houfek, Comput. Phys. Commun. **185**, 2893 (2014).
[41] F. Salvat, J. M. Fernández-Varea, and W. Williamson, Jr., Comput. Phys. Commun. **90**, 151 (1995).
[42] K. A. Berrington, W. B. Eissner, and P. H. Norrington, Comput. Phys. Commun. **92**, 290 (1995).

[43] M. K. Chen, Phys. Rev. A **56**, 4537 (1997).
[44] C. D. Lin, Phys. Rev. Lett. **51**, 1348 (1983).
[45] C. D. Lin, Phys. Rev. A **29**, 1019 (1984).
[46] C. D. Lin, Adv. At. Mol. Phys. **22**, 77 (1986).
[47] Y. Y. Qi, J. G. Wang, and R. K. Janev, Phys. Rev. A **80**, 063404 (2009).
[48] S. Kar and Y. K. Ho, Phys. Rev. A **83**, 042506 (2011).
[49] S. Kar and Y. K. Ho, Phys. Rev. A **79**, 062508 (2009).
[50] S. Kar, Y. Wang, Z. Jiang, S. Li, and K. Ratnavelu, Phys. Plasmas **21**, 012105 (2014).
[51] Z. Jiang, S. Kar, and Y. K. Ho, Phys. Plasmas **19**, 033301 (2012).
[52] S. Kar and Z. Jiang, At. Data Nucl. Data Tables **102**, 42 (2015).
[53] J. Berakdar and J. S. Briggs, J. Phys. B **27**, 4271 (1994).
[54] J. Berakdar and J. S. Briggs, J. Phys. B **29**, 2289 (1996).